ACADÉMIE
DES SCIENCES
INSTITUT DE FRANCE

Comptes Rendus
Chimie

Imen Dhifallah, Wafa Saadi and Souad Souissi-Najar

Kinetic, thermodynamic, and reaction mechanism study of raw *Phragmites australis* pyrolysis using thermogravimetric analysis

Volume 28 (2025), p. 275-288

Online since: 12 March 2025

https://doi.org/10.5802/crchim.379

This article is licensed under the
Creative Commons Attribution 4.0 International License.
http://creativecommons.org/licenses/by/4.0/

The Comptes Rendus. Chimie *are a member of the Mersenne Center for open scientific publishing*
www.centre-mersenne.org — e-ISSN : 1878-1543

ACADÉMIE DES SCIENCES
INSTITUT DE FRANCE

Comptes Rendus. Chimie
2025, Vol. 28, p. 275-288
https://doi.org/10.5802/crchim.379

Research article

Kinetic, thermodynamic, and reaction mechanism study of raw *Phragmites australis* pyrolysis using thermogravimetric analysis

Imen Dhifallah [*,a], **Wafa Saadi** [a] **and Souad Souissi-Najar** [a]

[a] Laboratory of Research: Process Engineering and Industrial Systems (LR11ES54), National School of Engineers of Gabes, University of Gabes, 6029 Gabes, Tunisia

E-mail: dhifallah.imen8@gmail.com (I. Dhifallah)

Abstract. The present study aimed at investigating the pyrolysis of *Phragmites australis* (PA) using non-isothermal thermogravimetric analysis (TGA) under nitrogen atmosphere at different heating rates (10, 20, 30, 40, and 50 °C/min). The activation energy values estimated using two models, Ozawa–Flynn–Wall and Kissinger–Akahira–Sunose, are approximately equal (156.98 kJ·mol^{-1} and 158.46 kJ·mol^{-1}, respectively), and the pre-exponential factor ranges between 2.37×10^{11} s^{-1} and 1.13×10^{12} s^{-1}. The reaction mechanism estimated based on the Coats–Redfern method indicates that the diffusion model (D3), as characterized by the Ginstling–Brounshtein equation, is the most appropriate mechanism in Region 1. However, in Region 2, the reaction mechanism can be described by two diffusion models: the Ginstling–Brounshtein (D3) and Valensi (D2) models.

Thermodynamic parameters, including enthalpy ΔH, Gibbs free energy ΔG, and entropy ΔS, are calculated (151.24 kJ/mol, 225.04 kJ/mol, and −94.49 J/(mol·K), respectively). They indicate the endothermic and non-spontaneous nature of the process and that the conversion of raw PA into bioenergy seems to be potentially viable and the product formation would be favorable. Therefore, raw PA appears to be an interesting material for conversion into bioenergy, activated carbon, and biochar synthesis used for liquid effluent treatment.

Keywords. Pyrolysis, TGA, Isoconversional models, Activation energy, Pre-exponential factor, Thermodynamic parameters, Coats–Redfern method.

Funding. Ministry of Higher Education and Scientific Research in Tunisia.

Manuscript received 29 June 2024, revised 31 October 2024 and 20 December 2024, accepted 16 January 2025.

1. Introduction

Biodegradable wastes, particularly lignocellulosic biomass, represent a promising sustainable energy source due to their abundance and renewability. This biomass, derived from agricultural residues and forestry byproducts, has garnered global interest due to its availability worldwide and its ability to be converted into various forms of bioenergy with net zero impact [1] by reducing greenhouse gas emissions [2] and substituting fossil fuels. It also contributes to waste management by repurposing materials that would otherwise be discarded [3]. Additionally, the processing of lignocellulosic biomass can promote rural development and a circular bioeconomy [4].

Advanced technologies, such as thermochemical conversion, are being explored to enhance the efficiency of converting lignocellulosic materials into bioenergy, making them a viable alternative to traditional energy sources [5]. Among these methods, pyrolysis is an environmentally friendly process in which the decomposition of organic material is conducted at temperatures ranging between 400 °C and 900 °C in the absence of oxygen [6]. It leads to the

* Corresponding author

formation of biogases (volatiles), bio-oil (liquid), and biochar (solid) [7]. Bio-oil is a highly promising biofuel that is used for heating and/or for power generation, but biochar can be used as soil amendment and soil carbon sequestration or to remove contaminants from the environment (water or gas treatment) [8].

Pyrolysis is considered a good waste processing method because it uses a wide variety of residues including agricultural residues [9], municipal solid waste [10], plastic waste [11], sludges [12], and so on. During pyrolysis, lignocellulosic biomass undergoes thermal degradation, leading to the release of volatile compounds and the formation of solid char residues [13].

Thermogravimetric analysis (TGA) is a pivotal technique for investigating the pyrolysis of lignocellulosic biomass, offering insights into the thermal stability and decomposition behavior of complex organic materials [14]. The TGA quantifies weight loss as a function of temperature, allowing for the determination of key parameters such as moisture content, ash yield, volatile matter, and fixed carbon contents [15,16]. By analyzing the thermal degradation profiles of biomass experimental data and the use of kinetic models, it is possible to calculate kinetic parameters such as the activation energy and the pre-exponential factor [17,18]; it is also possible to identify the pyrolysis mechanism and its thermodynamic parameters [19].

This analysis not only aids in optimizing pyrolysis processes for energy production but also enhances the understanding of product yields and the environmental implications of biomass utilization. Overall, TGA serves as an essential tool in the sustainable development of bioenergy from lignocellulosic materials [20].

Phragmites australis (PA) is one of the most widespread wetland plants globally, with significant biomass production due to its rapid growth and invasiveness [21,22]. Its ability to thrive in diverse environments has led to ecological concerns, particularly in regions where it outcompetes native species and disrupts ecosystems, impacting negatively the biodiversity [23,24], which makes its valorization in the pyrolysis process a promising approach to energy production and waste management [25,26].

Zhao et al. and Barbooti et al. investigated the thermal degradation of PA, and they found that this process occurs in three stages: the first stage corresponds to moisture evaporation; the second corresponds to the thermal degradation of cellulose, hemicellulose, and lignin; the third is characterized by the formation of fixed carbon and degradation of lignin, resulting in biochar formation and higher thermal stability [25,27]. To the best of our knowledge, the pyrolysis reaction mechanism of PA was investigated by some researchers using the master plot method, and there is no mention of the Coats–Redfern (CR) method for PA pyrolysis. This method is based on the application of heterogeneous reaction models (CR models) to the experimental data and compares the activation energy values obtained to those calculated with isoconversional models (Kissinger–Akahira–Sunose (KAS) and Ozawa–Flynn–Wall (OFW) models) to attain the best-fitted model and to predict the thermal degradation mechanism [28]. This method was used by Dhaundiyal and Gangwar [29] to investigate the pyrolysis mechanism of pine needles. Moreover, for instance, there is little information about the thermodynamic properties of the PA pyrolysis mechanism.

The main aim of the current work is to investigate the thermal behavior of Tunisian PA pyrolysis using experimental TGA data to obtain more information about kinetic and thermodynamic PA thermal degradation and the CR method to study this pyrolysis reaction mechanism. Besides, the climatic conditions in the Mediterranean basin and North Africa contribute to variations in biomass resource composition [30], which makes the focus on Tunisian PA pyrolysis critical to the development of localized biomass-to-energy conversion strategies.

2. Material and methods

2.1. *Preparation of raw and pyrolyzed biomass*

Phragmites australis was collected from Gabes, a region situated in the southern part of Tunisia. It was initially washed with distilled water several times to remove any impurities stuck to different plant parts. Then, the plant was dried in an air oven at 323 K for 48 h, crushed, and sieved to the desired particle size (ranging from 0.1 to 0.2 mm).

Raw PA pyrolysis was performed in a vertical cylindrical ceramic reactor with fixed parameters (nitrogen flow of 20 mL/min, heating rate of 10 °C/min, and 1 h of pyrolysis time) to evaluate its morphology and functional groups.

2.2. *Characterization of raw and pyrolyzed biomass*

2.2.1. *Morphology and composition of raw and pyrolyzed PA*

A scanning electronic microscope (SEM, type Tescan VEGA3 SBH model with tungsten filament) coupled to Bruker XFlash EDS sensor microanalysis for energy-dispersive X-ray (EDX) was used to examine the raw PA surface morphology (under 275× magnification) and to determine the percentage of some chemical elements (C, O, Na, Cl, and K).

The surface microstructure of the pyrolyzed PA was examined using an SEM (type FEIQ250/EDAX Thermo Fisher) under 2000× magnification.

Volatile matter (V_M) was obtained from the TGA data, and fixed carbon (F_C) content was calculated using this expression:

$$F_C\ (\%) = 100 - V_M\ (\%) - \text{moisture}\ (\%) - \text{ash}\ (\%) \quad (1)$$

2.2.2. *Determination of functional groups*

Raw and pyrolyzed PA functional group measurements were carried out with a Bruker ALPHA Fourier transform infrared (FTIR) spectrometer with a spectrum ranging between 400 cm^{-1} and 4000 cm^{-1}. The samples were prepared using the KBr method by Gardon et al. [31]. This technique involves mixing the powdered and dried samples with potassium bromide (KBr) in a ratio of about 1:100. The mixture is then placed into a pellet press; then, high pressure is applied to form a transparent pellet, which is analyzed in transmission mode.

2.3. *Thermogravimetric analysis*

The thermobalance SETARAM S60/58B41 was used to evaluate the weight loss of a definite mass of raw PA. Different heating rates (ranging from 10 °C/min to 50 °C/min) were applied to the PA samples under a fixed flow of inert gas (N_2) of 20 mL/min, and the results were presented as weight loss and derivative or differential thermogravimetric (DTG) curves for each heating rate.

2.4. *Kinetic modeling*

The TGA data of raw PA was used to study the thermal decomposition behavior during the pyrolysis process. The PA thermal degradation is considered a non-linear process composed of different stages, which can be described with various models. The Arrhenius law is used to analyze the PA pyrolysis as a function of thermal degradation time t [14,15,17]:

$$\frac{d\alpha}{dt} = K(T) f(\alpha) \quad (2)$$

where $f(\alpha)$ is the function of the reaction mechanism determined by the reaction type and α is the conversion rate described as

$$\alpha = \frac{m_0 - m}{m_0 - m_f} \quad (3)$$

where m_0 and m_f are the initial and the final mass, respectively, and m is the mass at a given time t (during thermal degradation).

$K(T)$ is the reaction rate constant, which can be defined by the Arrhenius law [14,15,17]:

$$K(T) = A \exp\left(-\frac{E_a}{RT}\right) \quad (4)$$

where E_a is the activation energy (kJ/mol), A is the pre-exponential factor (min^{-1}), R is the universal gas constant (8.314 J/mol·K), and T is the reaction temperature (K).

Equation (2) combined with Equation (4) gives

$$\frac{d\alpha}{dt} = A \exp\left(-\frac{E_a}{RT}\right) f(\alpha) \quad (5)$$

The integral form $g(\alpha)$ of the reaction model is

$$g(\alpha) = \int_0^\alpha \frac{d\alpha}{f(\alpha)} = \frac{A}{\beta} \int_{T_0}^{T} \exp\left(-\frac{E_a}{RT}\right) dT \quad (6)$$

where β is the heating rate (°C/min).

Some methods have been proposed to resolve Equation (6); among them is the CR method, which is used to estimate the reaction mechanism.

2.4.1. *Isoconversional models*

Isoconversional models are used to evaluate the activation energy for different values of the conversion rate. These models require that the kinetics of reactions do not depend on the heating rate, and then the conversion of raw materials into products takes place in a one-step process [7]. The temperature increases from T_0 with a constant heating rate β as described by these expressions:

$$T = \beta t + T_0 \quad (7)$$

$$dT = \beta\, dt \quad (8)$$

Combining these expressions with Equation (6) gives

$$g(\alpha) = \frac{AE_a}{\beta R}\int_x^{\infty} u^{-2}e^{-u}\,du = \frac{AE_a}{\beta R}P(x) \qquad (9)$$

where $P(x)$ is the temperature integral and has no analytical form and $x = E_a/RT$.

The KAS model. The KAS model represents all the chemical and physical reactions that take place during thermal decomposition. In this model, the temperature integral $P(x)$ is

$$P(x) = x^{-2}e^{-x} \qquad (10)$$

Then, Equation (9) becomes

$$\mathrm{Ln}\left(\frac{\beta}{T^2}\right) = \mathrm{Ln}\left(\frac{AE_a}{Rg(\alpha)}\right) - \frac{E_a}{RT} \qquad (11)$$

The activation energy can be calculated using the slope of the curve $\mathrm{Ln}(\beta/T^2)$ versus $(1/T)$ for different conversion rates.

The OFW model. The OFW model requires the measurement of temperatures corresponding to fixed conversion rates at different heating rates. In this case, the determination of activation energy does not require prior knowledge of reaction mechanisms [32].

This model, developed by Flynn and Wall [33] and Ozawa [34], uses a correlation among the heating rate, the activation energy, and the temperature of the samples during pyrolysis [7]. The derivation of this correlation is based on Doyle's approximation [35]:

$$\log(p(x)) \simeq -2.315 + 0.4567x \qquad (12)$$

Then, the OFW equation becomes

$$\mathrm{Ln}\beta = \mathrm{Ln}\left(\frac{AE_a}{Rg(\alpha)}\right) - 1.0516\frac{E_a}{RT} \qquad (13)$$

E_a is calculated using the slope of the plot $\mathrm{Ln}(\beta)$ versus $(1/T)$.

2.4.2. *Determination of the pre-exponential factor*

The pre-exponential factor (A) is an important parameter to obtain some information about the chemical reaction and then to optimize the pyrolysis. It can be calculated using this equation [36]:

$$A = \frac{\beta E_a}{RT_p^2}e^{E_a/RT_p} \qquad (14)$$

where T_p is the maximum peak temperature observed from the DTG curves.

2.5. *Thermodynamic parameters*

Enthalpy (ΔH), Gibbs free energy (ΔG), and entropy (ΔS) were calculated using kinetic data (E_a and A), TGA data points, and the following equations [37]:

$$\Delta H = E_a - RT \qquad (15)$$

$$\Delta G = E_a + RT_m \ln\left(\frac{K_B T}{h \cdot A}\right) \qquad (16)$$

$$\Delta S = \frac{\Delta H - \Delta G}{T_m} \qquad (17)$$

where T_m is the maximum temperature at which maximum decomposition is achieved, K_B is the Boltzmann constant (1.381×10^{-23} $m^2{\cdot}kg/s^2{\cdot}K^{-1}$), and h is the Planck constant (6.626×10^{-34} $m^2{\cdot}kg/s$).

2.6. *Estimation of the reaction mechanism*

The model developed by Coats and Redfern [28] is used to estimate the activation energy values by applying Equation (15) for the kinetic function corresponding to the appropriate pyrolysis mechanism.

$$\mathrm{Ln}\left[\frac{g(\alpha)}{T^2}\right] = \mathrm{Ln}\frac{AR}{\beta E_a}\left(1 - \frac{2RT}{E_a}\right) - \frac{E_a}{RT} \qquad (18)$$

Table 1 presents most of the solid-state degradation reactions and their functions $f(\alpha)$ and $g(\alpha)$. The E_a-value associated with each reaction mechanism is determined using the slope of the plot $\mathrm{Ln}(g(\alpha)/T^2)$ versus $1/T$. The appropriate reaction mechanism corresponds to the one that has the nearest E_a-value to those obtained with KAS and OFW models.

3. Results and discussion

3.1. *Characterization of raw and pyrolyzed PA*

3.1.1. *Composition of raw PA*

As illustrated in Figure 1, EDX analysis was conducted to identify some components present in the raw PA. The peaks show the prevalence of carbon and oxygen along with the presence of other components in trace amounts (Na, Cl, Si, Cl, and K). Table 2 presents an elemental composition of the raw PA added to ash, volatile matter, fixed carbon, and moisture content. High carbon and oxygen contents (47.35% and 48.58%, respectively) coupled with low moisture and ash contents (3.34% and 8.73%, respectively) indicate that this biomass is a highly promising raw material for a range of applications

Table 1. Reaction mechanisms functions, model names, and $f(\alpha)$ and $g(\alpha)$

Model name	$f(\alpha)$	$g(\alpha)$
Chemical reaction order		
Chemical reaction order 0 (F0)	1	α
Chemical reaction order 1 (F1)	$1-\alpha$	$-\mathrm{Ln}(1-\alpha)$
Chemical reaction order 1.5 (F1.5)	$(1-\alpha)^{3/2}$	$2[(1-\alpha)^{-3/2}-1]$
Chemical reaction order 2 (F2)	$(1-\alpha)^{2}$	$(1-\alpha)^{-1}-1$
Chemical reaction order 3 (F3)	$(1-\alpha)^{3}$	$[(1-\alpha)^{-2}-1]/2$
Chemical reaction order 4 (F4)	$(1-\alpha)^{4}$	$[(1-\alpha)^{-3}-1]/3$
Diffusion		
Parabolic law (D1)	$1/(2\alpha)$	α^{2}
Valensi equation (D2)	$-[\mathrm{Ln}(1-\alpha)]^{-1}$	$\alpha+(1-\alpha)\mathrm{Ln}(1-\alpha)$
Ginstling–Brounshtein equation (D3)	$(3/2)[(1-\alpha)^{1/3}-1]^{-1}$	$(1-2\alpha/3)-(1-\alpha)^{2/3}$
Jander equation (D4)	$(3/2)(1-\alpha)^{2/3}[1-(1-\alpha)^{1/3}]^{-1}$	$[1-(1-\alpha)^{1/3}]^{2}$
Nucleation and growth		
Avrami–Erofeev equation (N1.5)	$3(1-\alpha)[-\mathrm{Ln}(1-\alpha)]^{2/3}$	$[-\mathrm{Ln}(1-\alpha)]^{2/3}$
Avrami–Erofeev equation (N2)	$2(1-\alpha)[-\mathrm{Ln}(1-\alpha)]^{1/2}$	$[-\mathrm{Ln}(1-\alpha)]^{1/2}$
Phase interfacial reaction		
Shrinkage geometrical column (S1)	$2(1-\alpha)^{1/2}$	$1-(1-\alpha)^{1/2}$
Shrinkage geometrical spherical (S2)	$3(1-\alpha)^{2/3}$	$1-(1-\alpha)^{1/3}$

in energy, activated carbon, and biochar production processes. The composition of the PA Tunisian variety is close to the Egyptian PA reported by El Shahawy and Heikal [38]. Other biomasses observed in the literature like pine cones [13], olive stones [14], and cocoa shell [36] have high contents of volatile matter and fixed carbon and low ash content, which is important for gasification and pyrolysis processes. However, there are differences in composition, which may be due to species, variety, type of soil, or climatic conditions [39].

3.1.2. *Morphology of raw and pyrolyzed PA*

The SEM analysis of raw PA presented in Figure 2a shows that the biomass is rough with a regular and compact structure with fibers arranged in bundles [38]. The presence of a small number of pores and a cylindrical fiber structure gives the idea that the biomass has a typical compact lignocellulosic fibrous structure [40,41]. Ponce et al. [39] also revealed this structure for sugarcane bagasse, corn husk, and rice husk characterized by a cylindrical fiber with a rough structure.

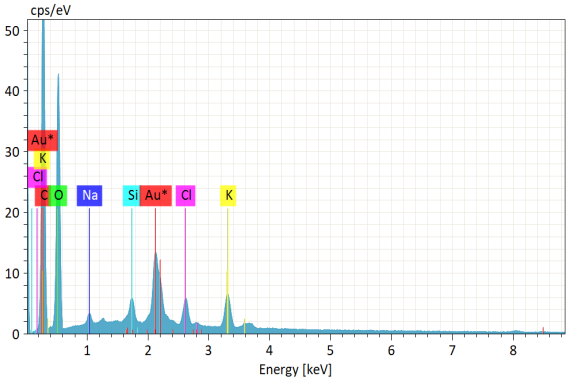

Figure 1. Energy-dispersive X-ray spectra of raw PA.

After pyrolysis, as shown in Figure 2b, the biochar develops a fairly high porosity, the surface morphology changes, and it becomes cleaner and fluffier than raw biomass. Many cracks, cavities, and spherical pores are also visible on the surface, but with different shades due to the loss of moisture and volatile matter. This structure is of great importance as it

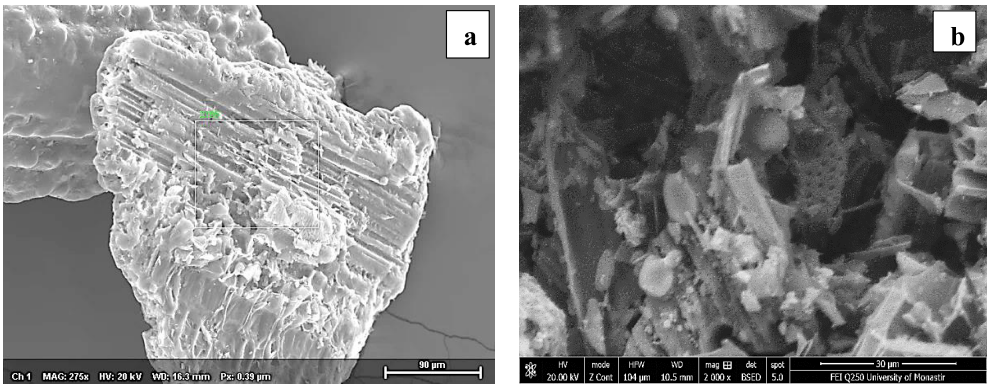

Figure 2. SEM of raw (a) and pyrolyzed (b) PA. (a) SE MAG: 275×, HV: 20 kV, WD: 16.3 mm; (b) SE MAG: 2000×, HV: 20 kV, WD: 10.5 mm.

Table 2. Composition of raw PA

Moisture (%)	Ash (%)	V_M (%)	F_C (%)	C (%)	O (%)	Na (%)	Si (%)	Cl (%)	K (%)
3.34	8.73	45.125	42.81	47.35	48.58	0.51	0.53	1.07	1.96

develops the PA pore structure, thereby enhancing the uptake of pollutants from aqueous solutions and the retention capacities of the biochar [8]. This structure was also observed by Kordoghli et al. [42] after orange peel pyrolysis and by Bouaik et al. [8] after red alga pyrolysis in which they have noticed the presence of pores with different forms (fluffy sponges, balls) and formless particles.

3.1.3. *Functional groups of raw and carbonized PA*

The FTIR analysis of raw and pyrolyzed PA is presented in Figure 3. The raw PA spectrum is similar to those obtained for other lignocellulosic materials such as olive stones, rice husk, sugarcane bagasse, and wheat straw [14,42].

The peak situated around 3128 cm^{-1} refers to the –OH stretching vibration of hydroxyl groups present in cellulose, hemicellulose, and lignin structures [43]. The C=O stretching vibrations at 1730 cm^{-1} can be assigned to carbonyl groups (ketones, phenols, carboxylic acids, and aldehydes) and confirm higher concentrations of lipids and fatty acids [44]. The band at 1603 cm^{-1} corresponds to the C–H deformation in methyl, methylene, and methoxyl groups of lignin [45]. The band observed at 1498 cm^{-1} is associated with lignin aromatic rings [40]. The peak at

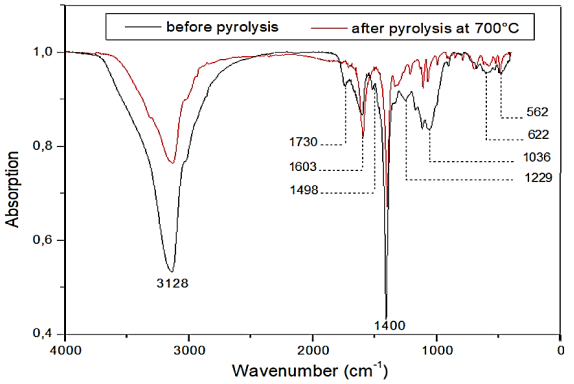

Figure 3. FTIR of raw and pyrolyzed PA before and after pyrolysis.

1400 cm^{-1} is due to the bending vibration of C–O–C pyranose ring skeletal vibration of cellulose present in the biomass [40]. The C–C ring breathing bands at 1229 cm^{-1} can be attributed to the presence of ether, ester, and phenol groups of lignin [45,46]. The band situated at 1036 cm^{-1} represents C–H or C–OH stretching vibration bonds in cellulose and hemicellulose [38] while the peaks appearing at 622 and 562 cm^{-1} are associated with bending vibrations of CH_3, $=CH_2$, and ≡CH, which are cellulose components [14]. Several biomasses such as pine cones [13]

and olive stones [14] present the same spectrum overall, which is explained by the primordial presence of cellulose, hemicellulose, and lignin in their structure, characteristic of lignocellulosic biomasses.

After pyrolysis, as shown in Figure 3, the O–H stretching bands located at 3128 cm^{-1} become significantly reduced because of the destruction of these groups as dehydration occurs and water is released as most of the organic oxygen-containing groups are broken [47]. It is also clear that the C=O stretching bands associated with carbonyl groups (at 1730 cm^{-1}) disappear because they are thermally decomposed [47]. The band situated at 1400 cm^{-1} presents a significant reduction, reflecting the destruction of glycosidic linkages [47].

Globally, a significant quantity of lignin, cellulose, and hemicellulose has been removed from the plant's structure during pyrolysis [48,49]. The same interpretation was developed by Tabal et al. [44] and Kordoghli et al. [41] who noticed that after the pyrolysis of Ficus wood and orange peels, several band intensities such as aliphatic remain weak or disappear due to organic decomposition in the presence of heat.

3.2. *Thermogravimetric analysis*

Thermogravimetric analysis is commonly employed to investigate the thermal composition of materials. The TG and DTG curves illustrating respectively the weight loss and derivative thermogravimetric variation as a function of temperature at different heating rates (10, 20, 30, 40, and 50 °C/min) are presented in Figure 4a and b. The shape of these curves is typical of the thermal degradation of lignocellulosic biomasses like olive stones [14], pomegranate peels [15], rice husk [50], cardoon leaves [51], and Typha latifolia [52], and they all reveal the presence of three stages of decomposition.

The first stage ranges from 350 K to 475 K for all the heating rates, and it is characterized by a small drop with a mass loss of about 2.35%, which corresponds to the evaporation of free physisorbed water in micropores and mesopores (moisture) [14]. The remaining low moisture makes the PA suitable for pyrolysis and combustion [53].

The second stage in which the most significant weight loss is observed (58.92%) and the temperature ranges between 475 K and 675 K indicates the

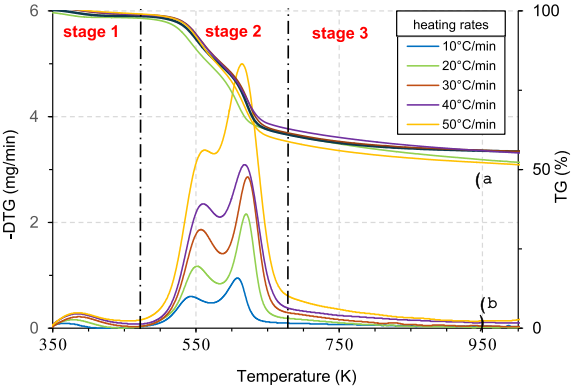

Figure 4. Weight loss (TG) (a) and differential thermogravimetric (DTG) (b) curves for different heating rates.

degradation of hemicellulose and cellulose present in the PA structure [54].

This stage in which the degradation of PA occurs is divided into two regions for all the heating rates. Region 1 (R1) characterized by the presence of a strong peak in the DTG curve situated at a temperature between 475 K and 575 K and by a conversion rate $\alpha \leq 0.35$ corresponds to the zone in which the hemicellulose is mainly pyrolyzed. Region 2 (R2) situated between 575 K and 675 K corresponds to the zone in which the cellulose is mainly pyrolyzed [14,15].

The third stage, observed at $T \geq 675$ K, presents a loss of weight of 8.97%, and it is associated with lignin decomposition [47]. The constant mass present in this stage is attributed to ash content representing the inorganic components present in PA [55].

Zhao et al. [56] revealed that PA pyrolysis occurs in three stages. The first stage involves the loss of cellular water (the temperature ranges between 323 and 513 K), and the second stage occurs as the temperature increases from 513 to 773 K and in which the major part of the organic material is decomposed (weight loss greater than 50%). This stage is divided into two regions: Region 1 in which the temperature increases from 513 to 591 K and Region 2 where the temperature increases from 591 to 773 K. The third stage is observed for a temperature over 773 K where there is a slight continued loss of weight which corresponds to a slow decomposition of residuals and carbonaceous matters present in the biomass.

Zhao et al. [27], who studied PA pyrolysis under different heating rates, also revealed the presence of

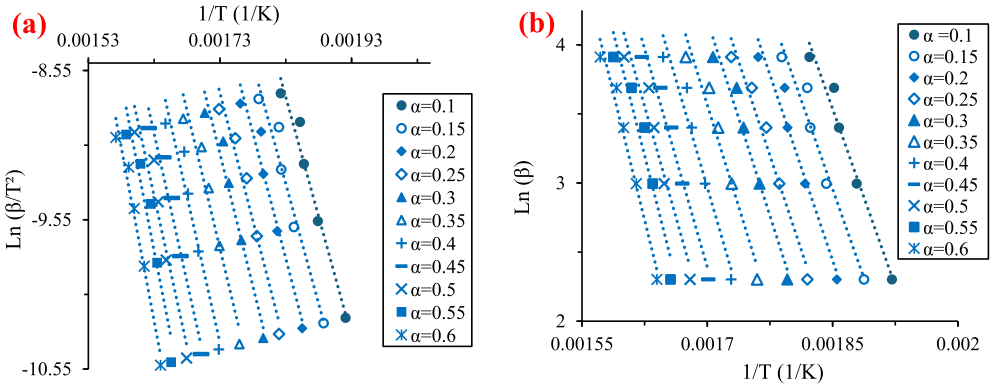

Figure 5. Linear fit plots of KAS (a) and OFW (b) models.

three stages (stage 1: from 313 to 422 K with 8% weight loss, stage 2: from 422 to 872 K with about 60% weight loss, and stage 3: from 872 to 1153 K with 4.65% weight loss).

When comparing these results, the presence of some similarities and differences attributed to the PA characteristics and origin, experimental conditions, and sample preparation is observed.

3.3. *Kinetic modeling*

3.3.1. *Evaluation of activation energy*

The plots corresponding to OFW and KAS models shown in Figure 5 (a and b, respectively) are used to estimate the activation energy of raw PA pyrolysis at conversion rates ranging between 0.1 and 0.6.

The results presented in Figure 6 show the dependence of activation energy on the conversion rate. The obtained values rise as the conversion rate values increase from around 133 kJ/mol for a conversion rate of 0.1 to nearly 193 kJ/mol for a conversion rate of 0.6. The lower E_a-value indicates that less energy was required to initiate a reaction, and then the energy increased as the reaction progressed [57]. This proves that pyrolysis is a multi-step process with various apparent activation energies [58]. Hemicellulose decomposition dominance in R1 requires less energy than cellulose decomposition, which is dominant in R2 [59]. In their investigation of olive kernel pyrolysis, Boukaous et al. [30] observed that the activation energies (E_a) increase with increasing conversion rates from approximately 170 kJ/mol to around 230 kJ/mol. This trend follows a similar E_a–α shape to that observed in PA pyrolysis studies. Besides,

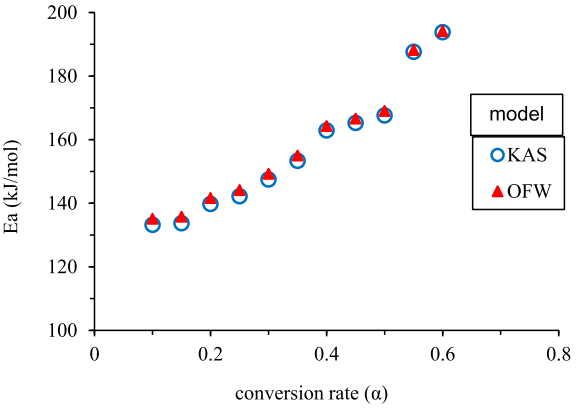

Figure 6. Variation of E_a-values with conversion rate for KAS and OFW models.

the values obtained with the two models are approximately equal with a minimal deviation of approximately 1%, confirming their validity (average E_a-value of 157.72 kJ/mol).

3.3.2. *Evaluation of the pre-exponential factor*

The pre-exponential factor is related to the reaction chemistry. In fact, lower A-values ($\leq 10^9$ s^{-1}) indicate a surface reaction, whereas higher values ($\geq 10^9$ s^{-1}) indicate a more complex reaction [52]. All the A-values calculated with the average E_a-value obtained from KAS and OFW models are presented in Table 3. They are above 10^9 s^{-1}, which shows the dominance of cellulose decomposition [60]. They also indicate the complexity of PA, the rotation of the active complex, and that the reagent remains constant during the monomolecular reactions of PA decomposition [61]. Moreover, these values are lower

Table 3. Pre-exponential factor for different heating rates

β (°C/min)	10	20	30	40	50	Average
A (s^{-1})	2.88×10^{11}	3.03×10^{11}	3.89×10^{11}	6.4×10^{11}	1.04×10^{12}	5.33×10^{11}

when compared to the A-values of Typha latifolia (A-values range from 5.53×10^{10} to 3.02×10^{15} s^{-1}) [52] and cocoa shell (A-values range from 4.26×10^{9} to 1.44×10^{15} s^{-1}) [36].

Table 4 groups together the kinetic parameter values obtained for various biomasses from the literature and those obtained in this work. They are well aligned and characteristic of lignocellulosic materials. When comparing the activation energy of PA (157.72 kJ/mol) with other biomasses, it falls into a moderate range, indicating that it requires a reasonable amount of energy for thermal breakdown. In contrast, materials like cardoon stems and maize cobs (224.51 kJ/mol and 202.19 kJ/mol, respectively) exhibit significantly higher activation energies, suggesting that they are more resistant to decomposition and may necessitate more intensive processing techniques. Conversely, biomasses such as pomegranate peels and olive stones (88.98 kJ/mol and 124 kJ/mol, respectively) have much lower activation energies, making them easier to convert into energy. This positions PA as a potentially efficient feedstock, requiring more energy than softer materials but less than highly fibrous substances, allowing for versatile application in various conversion processes while balancing energy requirements and processing costs.

3.4. *Thermodynamic parameters*

Enthalpy (ΔH), entropy (ΔS), and Gibbs free energy (ΔG) calculated for the different heating rates are presented in Table 5.

The positive ΔH-values indicate the endothermic nature of PA pyrolysis [64]. In fact, an external energy source is required to increase the energy level of the reagent and facilitate its transition [65]. The lower difference between E_a- and ΔH-values ($E_a - \Delta H \leq$ 6.5 kJ/mol) indicates that the pyrolytic conversion of PA into bioenergy seems to be potentially viable and the product formation would be favorable [52,66].

Barrier energy is represented by the low activation energy needed to break the chemical bonds found in organic molecules. Furthermore, it shows that the activation energy needed to break the chemical bonds in organic molecules and enable the synthesis of products seems to be low, indicating that the process might be completed with ease. This proves that the chemicals produced by pyrolyzing PA, such as coals, fuel gases, and bio-oils, are created without requiring a significant amount of extra heat. The efficient conversion of PA into bioenergy is shown by the preferential production of these products at lower enthalpy [52,67].

The parameter ΔG represents the amount of bioenergy that becomes available when pyrolysis occurs [67]. The ΔG-values of PA pyrolysis range between 218.54 and 233.29 kJ/mol, indicating the non-spontaneous nature of raw PA pyrolysis [52]. These values are higher when compared with Typha Latifolia (173–175 kJ/mol) [52], rice husk (143 kJ/mol), coffee husk (143 kJ/mol), groundnut shell (166.11 kJ/mol), and tea waste (169.238 kJ/mol) [4]. This indicates that the pyrolysis of PA will provide more energy than Typha latifolia, rice husk, coffee husk, groundnut shell, and tea waste.

The negative ΔS-values obtained in this study reveal that the decomposition of PA takes place at low speed [68], and it is also close to its thermodynamic equilibrium with higher thermodynamic stability [37]. This is confirmed by the results of the studies carried out by Mumbach et al. [36] on cocoa shell pyrolysis (ΔS-values between −39.51 and −72.7 J/mol.K) and Bongomin et al. [4] on rice husk pyrolysis (ΔS-value of −190.3 J/mol·K).

3.5. *Pyrolysis mechanism*

The CR method was used to estimate the raw PA pyrolysis mechanism. It is based primarily on tracing the plots of $\mathrm{Ln}(g(\alpha)/T^2)$ versus $1/T$ at all the heating rates (10, 20, 30, 40, and 50 °C/min) and for the two regions, R1 ($0.1 \leq \alpha \leq 0.35$) and R2 ($0.35 \leq \alpha \leq 0.6$). The slopes of these curves are used to calculate the activation energies for different reaction mechanism functions $g(\alpha)$ presented in Table 1.

Table 4. Activation energies and pre-exponential factors obtained for different biomasses

Biomass	E_a (kJ/mol)	A (s^{-1})	References
Phoebe zhennan wood	170.49	3.47×10^{17}	[2]
Cardoon stems	224.51	1.9×10^{19}	[7]
Olive stone	124	8.38×10^{8}	[14]
Pomegranate peels	88.98	3.41×10^{12}	[15]
Cocoa shell	104.5	2.74×10^{11}	[36]
Typha latifolia	183	1.5×10^{15}	[37]
Maize cob	202.19	8.14×10^{17}	[62]
Soybean straw	154.15	8.61×10^{14}	[63]
Phragmites australis	163–212.87	2.07×10^{10}	[27,56]
Phragmites australis	157.72	5.33×10^{11}	This work

Table 5. Thermodynamic parameters of PA pyrolysis

Heating rate (°C/min)	10	20	30	40	50	Average
ΔH (kJ·mol^{-1})	151.57	151.4	151.24	151.07	150.9	151.24
ΔG (kJ·mol^{-1})	218.54	220.57	224.25	228.59	233.29	225.04
ΔS (J·mol^{-1}·K^{-1})	−90.49	−91	−93.6	−96.89	−100.46	−94.49

Finally, the comparison between the obtained values and those calculated with the isoconversional models KAS and OFW helps to estimate the appropriate model. In fact, the E_a-values, which are nearly equal, show that this mechanism function is the best fit for the pyrolysis in this region. Figure 7 shows the plots obtained with different functions $g(\alpha)$ at a heating rate of 10 °C/min, and Table 6 regroups the E_a-values obtained from the slopes of these curves traced for all the heating rate values (from 10 to 50 °C/min).

In R1, the average E_a-value obtained from the application of the diffusion model D3 (about 136 kJ/mol) is the closest value to that obtained by KAS and OFW models (about 158 kJ/mol), with R^2 equal to 0.9737, which shows that three-dimensional diffusion is responsible for the reaction of pyrolysis in Region 1. In R2, E_a-values obtained from the diffusion models D2 and D3 are closest to the values obtained from KAS and OFW models, with an R^2-value nearly equal to 1. As a result, the most appropriate mechanism of raw PA pyrolysis in R2 is two- and three-dimensional diffusion described by Valensi and Ginstling–Brounshtein equations. Overall, the results suggest that PA pyrolysis is governed by diffusion mechanism across all regions. This mechanism is described as a solid-state reaction that often takes place between crystal lattices or with molecules that must enter lattices where motion is limited and may depend on lattice defects [2]. This result is also observed in the investigation conducted by Bongomin et al. [4] on the thermal behavior of coffee husk, ground shell, Macadamia nutshell, rice husk, and tea waste. They conclude that pyrolysis is predominately governed by different diffusion mechanisms in all regions, which reflect the complex thermal decomposition of these biomasses. A similar study was also conducted by Raza and Abu-Jdayil [69] on date seeds and cashew shells. They found that the pyrolysis mechanism of these biomasses is described by two diffusion models: Ginstling–Brounshtein and Jander models.

However, Mabrouki et al. [70] carried out a study on Ziziphus wood, date palm trunk, date palm leaflets, olive stones, vine stems, and almond shell. They reported that the pyrolysis of these biomasses could be described by a first-order chemical reaction model (F1) in R1 and second- and third-order chemical reaction models (F2, F3) in R2. Ahmad

Table 6. E_a- and R^2-values obtained for different reaction mechanisms using the CR method

Reaction model		10 °C/min		20 °C/min		30 °C/min		40 °C/min		50 °C/min		Average values	
		E_a (kJ/mol)	R^2	E_a (kJ/mol)	R^2	E_a (kJ/mol)	R^2	E_a (kJ/mol)	R^2	E_a (kJ/mol)	R^2	E_a (kJ/mol)	R^2
Reaction order													
R1	F0	54.766	0.962	60.926	0.966	62.997	0.967	59.096	0.961	56.68	0.979	58.893	0.967
	F1	62.83	0.972	69.773	0.976	72.121	0.976	67.731	0.972	69.391	0.976	68.369	0.974
	F1.5	76.316	0.984	84.57	0.986	87.388	0.977	82.172	0.979	84.162	0.987	82.921	0.982
	F2	0.505	0.289	1.248	0.634	1.48	0.727	0.856	0.373	0.939	0.489	1.005	0.502
	F3	6.465	0.929	7.786	0.934	8.225	0.943	7.23	0.909	7.463	0.926	7.433	0.928
	F4	12.505	0.941	14.413	0.942	15.062	0.947	13.686	0.927	14.072	0.937	13.947	0.938
R2	F0	27.355	0.998	29.652	0.991	30.869	0.988	30.294	0.991	44.997	0.957	32.633	0.985
	F1	42.053	0.973	45.237	0.984	47.04	0.985	46.264	0.988	50.292	0.985	46.177	0.983
	F1.5	70.823	0.986	75.722	0.973	78.696	0.977	77.523	0.979	83.722	0.973	77.297	0.977
	F2	11.955	0.892	13.087	0.856	13.89	0.883	13.528	0.885	33.863	0.824	17.264	0.868
	F3	33.116	0.925	35.458	0.9	37.172	0.917	36.514	0.918	39.538	0.902	36.359	0.912
	F4	59.316	0.932	63.538	0.908	44.365	0.947	65.374	0.925	70.328	0.909	60.584	0.924
Diffusion													
R1	D1	118.57	0.967	131.078	0.971	135.31	0.971	127.553	0.967	130.62	0.972	128.626	0.969
	D2	248.21	0.971	273.597	0.974	282.243	0.974	266.638	0.971	272.99	0.975	268.735	0.973
	D3	125.52	0.972	138.702	0.975	143.175	0.975	134.994	0.971	138.24	0.975	136.126	0.973
	D4	250.27	0.972	275.858	0.974	284.571	0.975	268.841	0.971	275.25	0.975	270.958	0.973
R2	D1	64.501	0.999	69.251	0.993	71.777	0.991	70.687	0.993	76.637	0.994	70.57	0.994
	D2	145.245	0.998	155.28	0.993	160.69	0.992	158.481	0.994	171.01	0.993	158.141	0.994
	D3	152.121	0.998	162.55	0.992	168.25	0.991	165.955	0.993	178.99	0.992	165.573	0.993
	D4	76.523	0.998	82.005	0.991	85.002	0.989	83.746	0.992	90.631	0.991	83.581	0.992
Nucleation and growth													
R1	N1.5	38.874	0.968	43.441	0.972	44.974	0.973	42.034	0.967	43.089	0.973	42.482	0.97
	N2	26.896	0.962	30.276	0.968	31.401	0.968	28.185	0.961	29.938	0.968	29.339	0.965
R2	N1.5	24.772	0.993	26.845	0.980	28.015	0.981	27.477	0.985	30.112	0.981	27.444	0.984
	N2	16.131	0.991	17.647	0.975	18.502	0.976	18.083	0.983	20.022	0.977	18.077	0.98
Phase interfacial reaction													
R1	S1	58.705	0.967	65.248	0.971	67.453	0.972	63.315	0.967	64.872	0.972	63.918	0.969
	S2	60.06	0.969	66.733	0.973	68.986	0.973	64.765	0.968	66.356	0.973	65.38	0.971
R2	S1	34.257	0.997	36.973	0.988	38.485	0.987	37.729	0.99	41.225	0.988	37.733	0.99
	S2	36.755	0.996	39.622	0.987	41.21	0.986	40.507	0.989	44.131	0.987	40.445	0.989

et al. [52], though, studied Typha latifolia pyrolysis; they showed that diffusion played a key role in Region 1, but Region 2 is governed by second- and third-order reaction models.

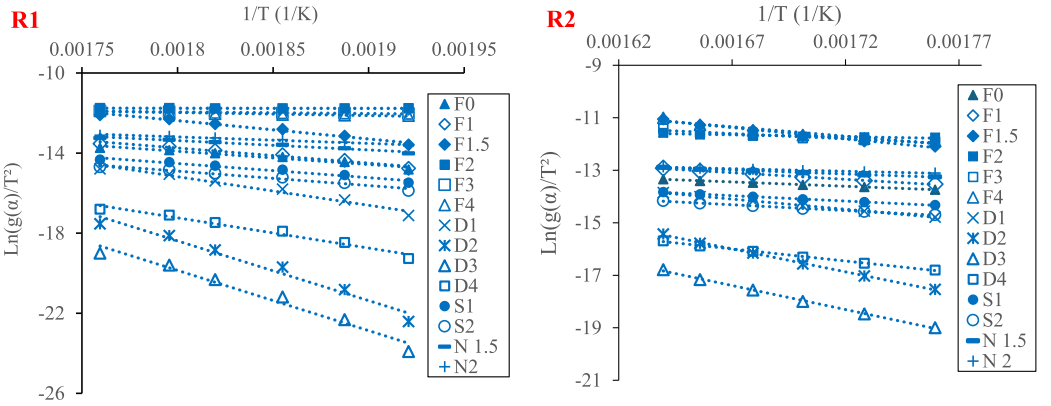

Figure 7. Coats–Redfern plots for pyrolysis of PA (for Regions R1 and R2 and $\beta = 10$ °C/min).

4. Conclusion

In this work, the pyrolysis behavior of *Phragmites australis* was investigated using TGA carried out at different heating rates (10, 20, 30, 40, and 50 °C/min). This analysis shows that PA pyrolysis occurs in three stages (the release of water molecules, hemicellulose and cellulose decomposition, and lignin decomposition). In addition, the activation energy values obtained by the OFW and KAS models are approximately equal, with a minimal deviation of approximately 1%, indicating high reliability of the results (with an average value of 157.72 kJ/mol). The pre-exponential factors obtained at different heating rates are in the range of 2.88×10^{11}–6.4×10^{11} s^{-1}, which shows the dominance of cellulose decomposition and the complexity of this biomass. Thermodynamic analysis shows that this reaction is endothermic, non-spontaneous, and it takes place at low speed and with high thermodynamic stability. Moreover, the CR method was used to estimate the reaction mechanism. It was found that the diffusion model (D3) characterized by the Ginstling–Brounshtein equation is the most appropriate mechanism in Region 1. However, in Region 2, the reaction mechanism can be described by two models: Ginstling–Brounshtein (D3) and Valensi (D2). All the results obtained from this study show that PA is an interesting source of thermal energy production. It is a promising energy feedstock and is also useful for biochar and activated carbon production with ecological and economic benefits, especially for liquid effluent treatment.

Greek symbols

α	conversion rate (–)
β	heating rate (°C·min^{-1})
ΔH	enthalpy variation (kJ·mol^{-1})
ΔG	Gibbs free energy (kJ·mol^{-1})
ΔS	entropy variation (J·mol^{-1}·K^{-1})

Nomenclature

A	pre-exponential factor (s^{-1})
CR	Coats–Redfern
DTG	derivative/differential thermogravimetric curve
E_a	activation energy (kJ·mol^{-1})
EDS	energy-dispersive X-ray
F_C	fixed carbon (%)
FTIR	Fourier transform infrared
$f(\alpha)$	function of reaction mechanism
$g(\alpha)$	complex integral function
h	Planck constant (1.38×10^{-23} m^2·kg/s^2·K^{-1})
KAS	Kissinger–Akahira–Sunose
K_B	Boltzmann constant (6.626×10^{-34} m^2·kg·s^{-1})
m_0	initial mass (kg)
m_f	final mass (kg)
m	mass at given time t (kg)
OFW	Ozawa–Flynn–Wall
PA	*Phragmites australis*
$P(x)$	temperature integral

R	universal gas constant (8.314 J·mol^{-1}·K^{-1})
R1	Region 1
R2	Region 2
SEM	scanning electronic microscope
T	temperature (°C)
T_0	initial temperature (°C)
T_f	final temperature (°C)
T_p	maximum temperature (°C)
TGA	thermogravimetric analysis
TG	weight loss
t	time (s)
V_M	volatile matter (%)

Declaration of interests

The authors do not work for, advise, own shares in, or receive funds from any organization that could benefit from this article, and have declared no affiliations other than their research organizations.

Acknowledgment

This work was supported by the Ministry of Higher Education and Scientific Research in Tunisia.

References

[1] J. Jin, Y. Li, J. Zhang, et al., *J. Hazard. Mater.* **320** (2016), pp. 417–426.
[2] H. Xiao, K. Jiang, Y. Chen, et al., *ACS Publ.* **5** (2020), pp. 20943–20952.
[3] M. Jeguirim, S. Jellali and B. Khiari, *C. R. Chim.* **25** (2022), pp. 1–5.
[4] O. Bongomin, C. Nzila, J. I. Mwasiagi and O. Maube, *Energy Convers. Manag.* **24** (2024), article no. 100723.
[5] G. Velvizhi, P. J. Jacqueline, N. P. Shetti, K. Latha, G. Mohanakarishma and T. M. Aminabhavi, *J. Environ. Manage.* **345** (2023), article no. 118527.
[6] N. Ferrera-Lorenzo, E. Fuente, I. Suárez-Ruiz, R. R. Gil and B. Ruiz, *J. Anal. Appl. Pyrolysis* **105** (2014), pp. 209–216.
[7] T. Damartiz, D. Vamvuka, S. Sfakiotakis and A. Zabaniotou, *Bioresour. Technol.* **102** (2011), pp. 6230–6238.
[8] H. Bouaik, A. Tabal, A. Barakat, K. El Harfi and A. Aboulkas, *C. R. Chim.* **24** (2021), pp. 85–99.
[9] S. Douvartzides, N. D. Charision, W. Wang, V. G. Papadakis, K. Polychronopoulou and M. A. Goula, *Renew. Energy* **185** (2022), pp. 483–505.
[10] Y. Du, T. Ju, Y. Meng, T. Lan, S. Han and J. Jiang, *Fuel Process. Technol.* **224** (2021), article no. 107026.
[11] T. Maqsood, J. Dai, Y. Zhang, M. Guang and B. Li, *J. Anal. Appl. Pyrolysis* **159** (2021), article no. 105295.
[12] S. Jellali, B. Khiari, M. Usman, H. Hamdi, Y. Charabi and M. Jeguirim, *Renew. Sustain. Energy Rev.* **144** (2021), article no. 111068.
[13] M. Boutaieb, M. Guiza, S. Román, B. L. Cano, S. Nogales and A. Ouederni, *C. R. Chim.* **23** (2020), pp. 607–621.
[14] A. Bedoui, S. Souissi-Najar and A. Ouederni, *Int. J. Innov. Appl. Stud.* **18** (2016), pp. 938–950.
[15] W. Saadi, S. Rodríguez Sanchez, B. Ruiz, S. Souissi-Najar, A. Ouederni and E. Fuente, *Renew. Energy* **136** (2019), pp. 373–382.
[16] A. Saddaoui, J. M. Jones, A. Williams and M. A. Wojtowicz, *Energy Fuels* **24** (2010), pp. 1274–1282.
[17] A. Bedoui, S. Souissi-Najar, S. S. Idris, N. Abd Rahman and A. Ouederni, *C. R. Chim.* **24** (2021), pp. 149–162.
[18] V. Ponnam, P. S. Tondepu and R. N. Mandapati, *J. Therm. Eng.* **7** (2021), pp. 18–29.
[19] J. Chen, Y. Wang, X. Lang, X. Ren and S. Fan, *Bioresour. Technol.* **241** (2017), pp. 340–348.
[20] J. Escalante, W. Chen, M. Tabatabaci and A. T. Hoang, *Renew. Sustain. Energy Rev.* **169** (2022), article no. 112914.
[21] O. Y. Farouk, J. R. Fahim, E. Z. Attia and M. S. Kamel, *S. Afr. J. Bot.* **163** (2023), pp. 659–672.
[22] K. L. Wilox, S. A. Petrie, L. A. Maynard and S. W. Meyer, *J. Great Lakes Res.* **29** (2003), pp. 664–680.
[23] B. Xiong, S. Han, T. C. Messerschmidt, M. L. Kirwan and K. Gedan, *Ecol. Indic.* **167** (2024), article no. 112651.
[24] O. A. Clevering and J. Lissner, *Aquat. Bot.* **64** (1999), pp. 261–273.
[25] M. Barbooti, F. K. Matlub and H. Hadi, *J. Anal. Appl. Pyrolysis* **98** (2012), pp. 1–6.
[26] L. G. Holm, D. L. Plucknet, J. V. Pancho and J. P. Herberger, *The World's Worst Weeds: Distribution and Biology*, University Press of Hawaii: Honolulu, Hawaii, 1977, p. 609.
[27] R. Zhao, L. Liu, Y. Bi, L. Tian and X. Wang, *Energy Convers. Manag.* **207** (2020), article no. 112510.
[28] A. W. Coats and J. P. Redfern, *Nat.* **201** (1964), pp. 68–69.
[29] A. Dhaundiyal and J. Gangwar, *Acta Univ. Sapientiae, Agric. Environ.* **7** (2015), pp. 5–22.
[30] N. Boukaous, L. Abdelouahed, M. Chikhi, C. Mohabeer, A. Hassen Meniai and B. Taouk, *C. R. Chim.* **23** (2020), pp. 623–634.
[31] S. H. Gordon, R. Kuru and A. Mohamed, *Talanta* **174** (2017), pp. 587–598.
[32] H. Aouled Mhemed, J. F. Largeau, S. Kordoghli, M. M. Gallego, F. Zagrouba and M. Tazerout, *Int. J. Biomass Renewab.* **9** (2020), pp. 25–41.
[33] J. H. Flynn and L. A. Wall, *Polym. Lett.* **4** (1966), pp. 323–328.
[34] T. Ozawa, *Bull. Chem. Soc. Jpn.* **38** (1965), pp. 1881–1886.
[35] C. D. Doyle, *J. Appl. Polym. Sci.* **5** (1961), pp. 285–292.
[36] G. D. Mumbach, J. L. F. Alves, J. C. G. da Silva, M. Di Domenico, R. F. de Sena, C. Marangoni, R. A. F. Machado and A. Bolzan, *Biomass Convers. Biorefin.* **12** (2022), pp. 723–739.
[37] Y. S. Kim, Y. S. Kim and S. H. Kim, *Environ. Sci. Technol.* **44** (2010), pp. 5313–5317.
[38] A. El Shahawy and G. Heikal, *RSC Chem.* **8** (2018), article no. 40511.
[39] J. Ponce, J. G. Andrade, L. N. dos Santos, et al., *Carbohydr. Polym. Technol. Appl.* **2** (2021), article no. 100061.

[40] G. B. Kankiliç and A. Metin, *J. Mol. Liq.* **312** (2020), article no. 113313.
[41] R. Dallel, A. Kesraoui and M. Seffen, *J. Environ. Chem. Eng.* **6** (2018), pp. 7247–7256.
[42] S. Kordoghli, E. Fassatoui, J. F. Largeau and B. Khiari, *C. R. Chim.* **26** (2023), pp. 37–51.
[43] A. A. Azzaz, S. Jellali, M. Jeguirim, L. Bousselmi, Z. Bengharez and H. Akrout, *C. R. Chim.* **24** (2021), pp. 71–84.
[44] A. Tabal, O. Belyazid, H. Dahman, E. Berrich, M. Jeguirim, M. El Achaby, K. El Harfi and A. Aboulkas, *C. R. Chim.* **26** (2023), pp. 7–23.
[45] C. Uma Maheswari, K. Obi Reddy, E. Muzenda, B. R. Guduri and A. Varada Rajulu, *Biomass Bioenergy* **46** (2012), pp. 555–563.
[46] Y. Li, Y. Liu, W. Chen, Q. Wang, Y. Liu, J. Li and H. Yu, *Green Chem.* **18** (2016), pp. 1010–1018.
[47] S. Suman, A. M. Yadav, T. Jain and A. Alisk, *Mater. Sci. Eng.* **1146** (2021), article no. 012023.
[48] B. Deepa, E. Abraham, N. Cordeiro, et al., *Cellulose* **22** (2015), pp. 1075–1090.
[49] D. Kim, B. Lee, D. Koo, P. Kang and J. Jeun, *Cellulose* **23** (2016), pp. 3039–3049.
[50] X. Cheng, Y. Tang, B. Wang and J. Jiang, *Waste Biomass Valor.* **9** (2018), pp. 123–130.
[51] M. H. Nabih, H. Boulika, M. El Hajam, N. I. Kandri, M. M. Alomran and F. Boufahja, *Open Chem.* **22** (2024), article no. 20240078.
[52] M. S. Ahmad, M. A. Mehmood, S. T. H. Taqvi, A. Elkamel, C. Liu, J. Xu, S. A. Rahimuddin and M. Gull, *Bioresour. Technol.* **245** (2017), pp. 491–501.
[53] R. M. Braga, D. M. A. Melo, F. Aquino, J. C. Freitas, M. A. F. Melo, J. M. F. Barros and M. S. B. Fonte, *J. Therm. Anal. Calorim.* **115** (2014), pp. 1915–1920.
[54] A. Anca-Couce, *Prog. Energy Combust. Sci.* **53** (2016), pp. 41–79.
[55] T. Sitek, J. Pospisil, J. Polacik and R. Chylek, *Energy* **237** (2021), article no. 121609.
[56] H. Zhao, H. Yan, C. Zhang, X. Liu, Y. Xue, Y. Qiao, Y. Tian and S. Qin, *Evid Based Complement Alternat. Med.* **2011** (2011), article no. 408973.
[57] J. Huang, J. Zhang, J. Liu, et al., *J. Anal. Appl. Pyrolysis* **139** (2019), pp. 177–186.
[58] K. Açıkalın, *Bioresour. Technol.* **337** (2021), article no. 125438.
[59] B. Nath, G. Chen, L. Bowtell and E. Graham, *Heliyon* **9** (2023), article no. e20602.
[60] Y. Lin, J. Cho, G. A. Tompsett, P. R. Westmoreland and G. W. Huber, *J. Phys. Chem.* **46** (2009), pp. 20097–20107.
[61] Y. Xu and B. Chen, *Bioresour. Technol.* **146** (2013), pp. 485–493.
[62] D. K. Okot, P. E. Bilsborrow, A. N. Phan and D. A. C. Manning, *Heliyon* **9** (2023), article no. e17236.
[63] X. Huang, J. Cao, X. Zhao, J. Wang, X. Fan, Y. Zhao and X. Wei, *Fuel* **169** (2016), pp. 93–98.
[64] D. E. Daugaard and R. C. Brown, *Energy Fuels* **17** (2003), pp. 934–939.
[65] L. Huang, J. Liu, Y. He, et al., *Bioresour. Technol.* **218** (2016), pp. 631–642.
[66] G. D. Mumbach, J. L. F. Alves, J. C. G. Da Silva, R. F. De Sena, C. Marangoni, R. A. F. Machado and A. Bolzan, *Energy Convers. Manage.* **200** (2019), article no. 112031.
[67] L. Vlaev, V. Georgieva and S. Genieva, *J. Therm. Anal. Calorim.* **88** (2007), pp. 805–812.
[68] J. M. Rami, C. D. Patel, C. M. Patel and M. V. Patel, *Mater. Today Proc.* **43** (2021), pp. 655–659.
[69] M. Raza and B. Abu-Jdayil, *Case Stud. Therm. Eng.* **47** (2023), article no. 103118.
[70] J. Mabrouki, M. A. Abbassi, B. Khiari, S. Jellali and M. Jeguirim, *C. R. Chim.* **25** (2022), pp. 81–92.